

Emission characteristics of quantum dots in planar microcavities

G. Ramon,^{1,*} U. Mizrahi,² N. Akopian,² S. Braitbart,²
D. Gershoni,² T. L. Reinecke,¹ B. Gerardot,³ and P. M. Petroff³

¹*Naval Research Laboratory, Washington DC 20375-5320*

²*The Physics Department and the Solid State Institute,*

Technion – Israel Institute of Technology, Haifa 32000, Israel

³*Materials Department, University of California Santa Barbara, CA, 93106*

The emission properties of single quantum dots in planar microcavities are studied experimentally and theoretically. Fivefold Enhanced spontaneous emission outside the microcavity is found for dots in resonance with the cavity mode, relative to detuned dots, while their radiative lifetime is only marginally decreased. Using high power excitation we obtain the in-plane cavity dispersion. Near field images of the emission show spatial distributions of several microns for resonant dots, which decrease in size with the detuning from resonance. These experimental findings are explained using a simple and intuitive model.

PACS numbers: 03.67.-a, 78.67.Hc, 73.21.La, 78.55.Cr

I. INTRODUCTION

The potential applications of semiconductor quantum dots (QDs) as quantum light emitters have generated considerable research efforts in recent years.¹ Single photon sources using quantum dots are an important ingredient in quantum information applications such as quantum cryptography and teleportation,² and may be further employed to implement efficient linear optics quantum computation³ with the attainment of on-demand indistinguishable single-photon pulses.⁴ Single QDs can be excited either with continuous wave (cw), where they emit antibunched photons obeying a sub-Poissonian statistics or with pulsed light, where a single photon is emitted per pulse.¹ It is the radiative recombination of electron-hole (e-h) pairs (or excitons) confined in single QDs that gives rise to the emission of single photons.

QD based devices have several advantages as single photon emitters. These include relatively large oscillator strengths, narrow spectral linewidths, and compatibility with mature semiconductor technologies. A major hindrance in their usefulness, though, is the low extraction efficiency of the emitted photons due to the high refraction index of the host semiconductor. Typically, only about two percent of the photons will be emitted from a GaAs based device, while the rest will be lost due to total internal reflection. The general approach to overcome this problem has been to place the QDs at the antinode of a microcavity whose dimensions are comparable to the wavelength of the emitted photons.⁵ In these cavities the number of allowed optical modes is reduced and at the same time, the in-cavity intensity of the allowed modes increases. As a result, the spontaneous recombination rate of excitons within these resonating modes is increased, a phenomenon known as the Purcell effect.^{6,7}

Several approaches to realize 3D photon confinement have been studied, including whispering-gallery modes in microdisks,⁸ defect modes in 2D photonic crystals,⁹ and lateral patterning of planar dielectric cavities using

electron-beam lithography and etching.^{7,10} The latter has proved particularly useful, demonstrating efficient photon emission in the weak coupling regime,⁷ and more recently strong coupling, paving the pathway for solid state realization of coherent control schemes.¹⁰ In the strong coupling regime, the interaction between the cavity mode and the emitter is larger than their combined decay rates, and the irreversible spontaneous emission from the QD exciton is replaced by a coherent exchange of energy between the exciton and the cavity mode. Among the challenges in the implementation of strong coupling in structured cavities, one notes the reduction in the cavity's Q-factor due to the lateral patterning, and the lack of control in the in-plane positioning of the QD with respect to the lateral microstructure, resulting in a reduction in the oscillator strength of the confined exciton.^{10,11}

In view of the technological difficulties associated with systems of QDs in 3D cavities, it seems important to study a system of QDs embedded in a planar microcavity, which is easier to fabricate. These cavities consist of distributed Bragg reflectors (DBRs), which are typically stacks of alternating quarter-wavelength-thick layers of GaAs and AlAs, separated by a spacer layer of GaAs. Planar cavities can attain high Q factors due to the excellent control in their fabrication and embedding the QDs at the field's antinode is straightforward. These structures support an in-plane continuum of modes, and the interaction with QD excitons is therefore not expected to be in the strong coupling regime.¹² Nevertheless, the spontaneous emission and the light extraction efficiency can still be enhanced considerably.¹³ For example, a relatively weak planar cavity has been utilized recently to produce a ten-fold increase in the efficiency of light collection of GaAs based LED structures.¹⁴

Unlike systems of quantum wells embedded in planar cavities, where polariton effects prevail and have been extensively studied (see e.g.,^{15,16,17,18}), QDs in planar cavities have received little attention.^{19,20} Among the few experimental studies of this system, angle-resolved photoluminescence spectroscopy was used to detect TE-

TM mode splitting (not to be confused with Rabi splitting, which is discernable only in the strong coupling regime).²¹

In the present work we study experimentally and theoretically single QD emitters in a planar microcavity. Using a partially covered layer of InGaAs self assembled QDs placed at the center of a λ microcavity, we have measured various characteristics of the spontaneous emission dynamics of the system such as spatial and angular distributions of the radiation field and its temporal decay. Our results are compared with a relatively simple theoretical analysis, which follows the treatment of Sugawara¹⁹ and gives a simple and intuitive picture of the spontaneous emission properties of recombining excitons confined in QDs embedded in a planar microcavity. This approach accounts reasonably well for our experimental findings, including emission rates, radiative lifetimes, and angular and spatial distributions of the emission. In all of these measurements, a crucial parameter is found to be the detuning of the emitter energy from that of the cavity resonant mode. Since we do not have an exact knowledge of the QDs size, shape and composition, detuning from resonance is modeled in our approach by either varying the QD size or by varying its material bandgap, while keeping the optical properties of the microcavity fixed.

The paper is organized as follows. In section II we provide the details of our experimental system. Section III gives the theoretical model including the exciton wavefunctions and their interaction with the cavity field. In section IV we give the experimental measurements and compare them with model calculations. A summary is given in section V, and some details pertaining to the calculation of the excitonic wavefunction are given in the appendix.

II. EXPERIMENTAL SETUP

The samples were grown by molecular beam epitaxy on a (100) oriented GaAs substrate. One layer of strain-induced InGaAs QDs was deposited in the center of a one wavelength GaAs spacer layer. The height and composition of the QDs were controlled by partially covering the InAs QDs by 30Å thick layer of GaAs and by subsequent two minutes growth interruption²² to allow diffusion of In (Ga) atoms from (into) the strained islands. The growth resulted in $\text{In}_x\text{Ga}_{1-x}\text{As}$ QDs whose estimated radius and composition are $150\text{Å} \lesssim R_{\text{QD}} \lesssim 250\text{Å}$ and $0.47 \lesssim x \lesssim 0.53$, respectively, and height of 30Å. The GaAs spacer layer was grown to a width whose resonance mode matches the QDs emission due to ground state e-h pair recombinations (1 λ cavity). The microcavity was formed by 25 and 11 period stacks of alternating quarter wavelength layers of AlAs and GaAs below and above the spacer layer, respectively. The samples were not patterned or processed laterally to prevent obscuring the emission and its polarization.

For the optical measurements we used a diffraction lim-

ited low temperature confocal optical microscope^{31,32}. The sample was cooled by a copper braid attached to the cold finger of a He-flow cryostat. The sample mount was accurately manipulated in three directions using computer-controlled motors. A X60 in-situ microscope objective was used in order to focus cw or pulsed laser light at normal incidence on the sample. The emitted light was collected by the same microscope objective. The collected light was spatially filtered, dispersed by a 0.22 m monochromator and detected by a nitrogen-cooled CCD array detector. The system provides diffraction-limited spatial resolution, both in the excitation and the detection channels. For the time-resolved spectroscopy, the dispersed light from the monochromator was focused onto a small, thermoelectrically cooled, single channel avalanche silicon photodiode. The signal from the photodiode was analyzed using conventional photon counting electronics. The photodiode dark count rate was 100 sec^{-1} , and the system temporal resolution was approximately 250 psec.

III. THEORETICAL FRAMEWORK

The following approach assumes a single 1s exciton confined in a QD interacting with a discrete cavity mode. No charged exciton or biexciton states were considered, although their presence was confirmed in the measurements (see section IV A). Our main interest in the current study is in the cavity effects on the excitons emission dynamics. The assumption of discrete cavity modes is justified for high finesse cavities. (we have verified that only the basic λ mode contributes appreciably to the interaction with the exciton). Although more complete description of the electromagnetic density of states in the cavity is available¹⁷, the main features of the exciton-photon coupling are well demonstrated within the framework of our simplified model.

A. Model wavefunction for quantum dot excitons

We start by solving for the excitonic wave function in a quantum dot, considering finite potential barrier in the growth (z) direction and parabolic potential in the lateral direction.

The effective mass Hamiltonian is given by

$$H = -\frac{\hbar^2}{2m_e^{\parallel}} [\nabla_{\rho_e}^2 + \sigma \nabla_{\rho_h}^2 + \sigma_{ez} \partial_{z_e}^2 + \sigma_{hz} \partial_{z_h}^2] - \frac{e^2}{\epsilon \sqrt{(\rho_e - \rho_h)^2 + (z_e - z_h)^2}} + V_e(\rho_e, z_e) + V_h(\rho_h, z_h), \quad (1)$$

where $\mathbf{r}_i = (\rho_i, z_i)$ are the electron or hole in-plane and z coordinates, and $\sigma = m_e^{\parallel}/m_h^{\parallel}$, $\sigma_{ez} = m_e^{\parallel}/m_e^z$, $\sigma_{hz} = m_e^{\parallel}/m_h^z$ are the appropriate effective mass ratios in the

plane and z directions, and ϵ is the background dielectric constant screening the Coulomb interaction. In Eq. (1) we have neglected the differences in the conduction- and valence-band masses and in the dielectric constant value of the two semiconductors that comprise the QD and its host. In the case of strong z direction confinement, the electron and hole potentials can be approximated as

$$V_i(\boldsymbol{\rho}_i, z_i) \approx V_i(\boldsymbol{\rho}_i) + V_i(z_i), \quad i = e, h \quad (2)$$

thus decoupling the problem into lateral and z parts, and enabling us to write the envelope wave function for the exciton in the form

$$\Phi_{\mathbf{x}}(\mathbf{r}_e, \mathbf{r}_h) = \Psi_{\mathbf{x}}(\boldsymbol{\rho}_e, \boldsymbol{\rho}_h) \chi_e(z_e) \chi_h(z_h) \quad (3)$$

(for infinite z direction potential, this approximation is exact). Transforming to center of mass (CM) and relative in-plane coordinates:

$$\mathbf{R} = \frac{\sigma \boldsymbol{\rho}_e + \boldsymbol{\rho}_h}{1 + \sigma}; \quad \mathbf{r} = \boldsymbol{\rho}_e - \boldsymbol{\rho}_h, \quad (4)$$

we separate the CM-motion and relative-motion wave functions, $\Psi_{\mathbf{x}}(\mathbf{R}, \mathbf{r}) = \psi(\mathbf{R})\phi(\mathbf{r})$, by Choosing parabolic potentials for the lateral confinement of both electron and hole^{23,24}

$$V_i(\boldsymbol{\rho}_i) = \frac{1}{2} m_i^{\parallel} \omega^2 \rho_i^2, \quad i = e, h. \quad (5)$$

Employing natural units of length and energy, namely, bulk effective Bohr radius ($a_B = \hbar^2 \epsilon / m_e^{\parallel} e^2$) and Rydberg ($\text{Ry} = \hbar^2 / 2m_e^{\parallel} a_B^2$), the Hamiltonian in Eq. (1) takes the form

$$\begin{aligned} H &= H_R + H_r, \\ H_R &= -\frac{\sigma}{1 + \sigma} \nabla_R^2 + \frac{4\sigma R^2}{\xi^4 (1 + \sigma)} \\ H_r &= -\left[(1 + \sigma) \nabla_r^2 + \sigma_{ez} \partial_{z_e}^2 + \sigma_{hz} \partial_{z_h}^2 \right] - \\ &\quad \frac{2}{\sqrt{r^2 + (z_e - z_h)^2}} + \frac{4\sigma^2 r^2}{\xi^4 (1 + \sigma)^3} + V_e(z_e) + V_h(z_h) \end{aligned} \quad (6)$$

where ξ is a dimensionless lateral localization parameter related to the confining potential by

$$\xi = \frac{1}{a_B} \sqrt{\frac{2\hbar}{M_x \omega}} \quad (7)$$

and $M_x = m_e^{\parallel} + m_h^{\parallel}$ is the in-plane CM exciton mass.

We identify the in-plane CM motion part with a 2D harmonic oscillator Hamiltonian, which is solved analytically resulting in wave functions $\psi(\mathbf{R})$ which are given by the associated Laguerre polynomials²⁵. In what follows, we will be interested only in the CM-motion ground state which is a 2D Gaussian function. By equating the areal size of the CM wave functions with the physical QD radius: $|\int \psi(\mathbf{R}) d^2 R|^2 = 2\pi \xi^2 = \pi R_D^2$, we relate the potentials (5) with the QD size.

For the in-plane relative coordinates we employ a trial wave function²⁵

$$\phi(r) = \mathcal{N}_r e^{-(r/\eta)^\alpha} \quad (8)$$

where \mathcal{N}_r is a normalization constant and η, α are variational parameters. α has values between 1 (no lateral confinement - very large QDs) and 2 (strong lateral confinement - very small QDs). Considering finite height potentials in the z direction, $V_i(z_i) = V_i^z \Theta(|z_i| - L/2)$ where $i = e, h$ and L is the QD height, we have for the z wave functions^{26,27}

$$\chi_i(z_i) = \mathcal{N}_{z_i} \times \begin{cases} \cos(k_i z_i) & |z_i| \leq L/2 \\ \frac{k_i}{\sqrt{k_i^2 + \kappa_i^2}} e^{-\kappa_i (|z_i| - L/2)} & |z_i| > L/2 \end{cases} \quad (9)$$

where $i = e, h$, $\mathcal{N}_{z_i} = (L/2 + 1/\kappa_i)^{-1/2}$ is a normalization constant,

$$k_i = \sqrt{\frac{2m_i^z}{\hbar^2} E_{i0}^z}, \quad \kappa_i = \sqrt{\frac{2m_i^z}{\hbar^2} (V_i^z - E_{i0}^z)}, \quad (10)$$

and E_{i0}^z is determined by the ground state quantization condition:

$$\sqrt{\frac{E_{i0}^z}{V_i^z}} = \cos\left(\frac{L}{2} \sqrt{\frac{2m_i^z}{\hbar^2} E_{i0}^z}\right). \quad (11)$$

The variational parameters in Eq. (8) are calculated by maximizing the magnitude of the ground state exciton binding energy $E_B = E_{e0}^z + E_{h0}^z + E_{1s}^{\text{CM}} - E_r$, where $E_{1s}^{\text{CM}} = \hbar\omega = \frac{4\sigma}{\xi^2(1+\sigma)}$ is the ground state energy of the CM motion and E_r is the expectation value of the relative motion part of the Hamiltonian in (6) (see Appendix).

The InGaAs self-assembled QDs that we are considering have an estimated height of $L = 30\text{\AA}$. The conduction- and valence-band in-plane and normal to the plane masses were calculated for this quantum well width, assuming 50% InAs contents, using an eight band Kane model, and taking into account both non-parabolicity and lattice-mismatch strain effects.²⁸ We find for the electron: $m_e^{\parallel} = 0.0630$, $m_e^z = 0.0897m$, and for the heavy hole: $m_h^{\parallel} = 0.1573m$, $m_h^z = 0.3406m$. For the potential barriers we find: $V_e^z = 441.9\text{meV}$ and $V_h^z = 110.6\text{meV}$. Using these values we minimize Eq. (A-1) with respect to the two variational parameters α and η , and find the binding energy of the ground state heavy-hole exciton as a function of the QD radius shown in figure 1.

B. Exciton-photon interaction in a planar microcavity

In the following we assume weak coupling between the QD exciton and the cavity modes. This is justified a-posteriori by the calculated spontaneous emission linewidths, which are always much smaller than that of

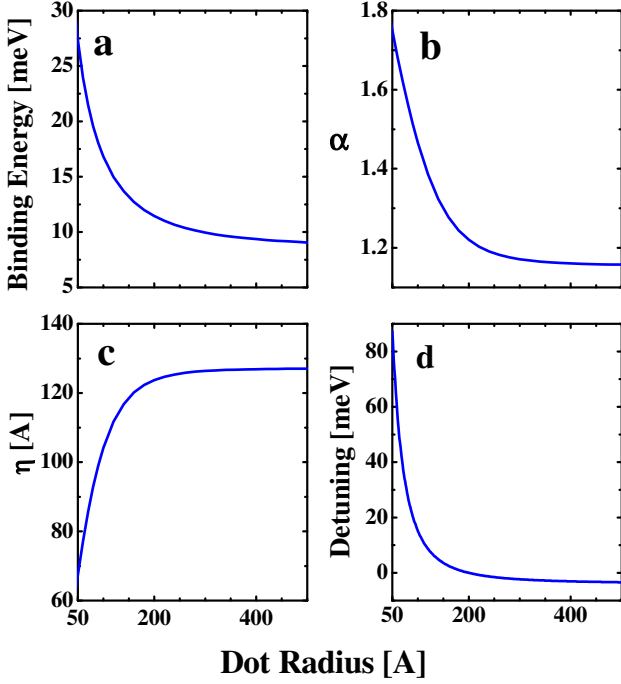


FIG. 1: (a) Exciton binding energy, (b) Variational parameter α , (c) Variational parameter η , and (d) Detuning of the exciton line with respect to the cavity mode, as functions of the QD radius (resonance was assumed for $R_D = 200\text{\AA}$).

the cavity. The cavity photon escape rate was deduced from the measured reflectivity of the cavity. We have put the cavity structure into a linear dispersion model and calculated its reflectivity using transfer matrix formalism. The resulting cavity mode linewidth was close to the measured value.

The interaction between an exciton and the electromagnetic field is given by

$$H_{\text{int}} = -\frac{e}{mc} \sum_{\mathbf{k}, \sigma} \mathbf{p} \cdot \mathbf{A}_{\mathbf{k}}^{\sigma} \quad (12)$$

where $\mathbf{A}_{\mathbf{k}}^{\sigma}$ is the vector potential associated with the k th mode with polarization σ and we have neglected the quadratic term in \mathbf{A} . In a planar cavity, with z in the growth direction, the Maxwell equations with the appropriate boundary conditions yield two solutions for the electromagnetic field.²⁹ These correspond to the electric vector being normal to (TE) or in (TM) the plane defined by the wave vector $\mathbf{k} = (\mathbf{k}_{\parallel}, k_z)$ and z , and are

given (using the Coulomb gauge) by:

$$\begin{aligned} \mathbf{A}_{\mathbf{k}}^{\text{TE}} &= -i\sqrt{\frac{2\pi\hbar v}{kV_c}} \cos(k_z z) \mathbf{e}_{\parallel} \left[e^{i\mathbf{k}_{\parallel} \cdot \boldsymbol{\rho}} \hat{a}_{\mathbf{k}} + e^{-i\mathbf{k}_{\parallel} \cdot \boldsymbol{\rho}} \hat{a}_{\mathbf{k}}^{\dagger} \right] \quad (13a) \\ \mathbf{A}_{\mathbf{k}}^{\text{TM}} &= \sqrt{\frac{2\pi\hbar v}{kV_c}} \left[-i\frac{k_z}{k} \cos(k_z z) \mathbf{e}_{\parallel} + \frac{k_{\parallel}}{k} \sin(k_z z) \mathbf{e}_{\perp} \right] \times \\ &\quad \left[e^{i\mathbf{k}_{\parallel} \cdot \boldsymbol{\rho}} \hat{a}_{\mathbf{k}} + e^{-i\mathbf{k}_{\parallel} \cdot \boldsymbol{\rho}} \hat{a}_{\mathbf{k}}^{\dagger} \right] \quad (13b) \end{aligned}$$

where $v = c/n_{\text{eff}}$ is the velocity of light in the cavity medium, V_c is the cavity quantization volume, and $\hat{a}_{\mathbf{k}}^{\dagger}$ ($\hat{a}_{\mathbf{k}}$) is the creation (annihilation) operator of the \mathbf{k} field mode. In Eqs. (13) k_z satisfies the resonance condition

$$k_z = \frac{2m\pi}{L_c}, \quad (14)$$

where m takes any integer value and L_c is the cavity width. Here we have considered only even modes which are the only ones which couple with the exciton ground state.¹⁶ Assuming a system of a single exciton and a single photon, appropriate for low exciton densities, the time-dependent state of the system is given by

$$|\Psi(t)\rangle = b(t)e^{-i\omega_x t} |\Phi_x, 0\rangle + \sum_{\mathbf{k}, \sigma} c_{\mathbf{k}, \sigma}(t) e^{-i\omega_{\mathbf{k}} t} |\Phi_g, 1_{\mathbf{k}, \sigma}\rangle \quad (15)$$

where ω_x ($\omega_{\mathbf{k}}$) is the exciton (electromagnetic field) resonant frequency, and σ runs over the two light polarizations. Taking the system to be initially with one exciton and the radiation field in the vacuum state [$b(0) = 1$, $c_{\mathbf{k}, \sigma}(0) = 0$] we write the equations of motion for $b(t)$ and $c_{\mathbf{k}, \sigma}(t)$, using the rotating wave approximation:

$$\dot{b}(t) = -i \sum_{\mathbf{k}, \sigma} g_{\mathbf{k}, \sigma} e^{i(\omega_x - \omega_{\mathbf{k}})t} c_{\mathbf{k}, \sigma}(t) - \frac{\gamma_x}{2} b(t) \quad (16a)$$

$$\dot{c}_{\mathbf{k}, \sigma}(t) = -ig_{\mathbf{k}, \sigma}^* e^{-i(\omega_x - \omega_{\mathbf{k}})t} b(t) - \frac{\gamma_c}{2} c_{\mathbf{k}, \sigma}(t). \quad (16b)$$

In Eqs. (16) γ_x is the exciton broadening due to all processes other than spontaneous emission (phonon scattering, nonradiative recombination), and γ_c is the decay rate of the cavity photon mode due to mirror losses, which is inversely proportional to the cavity quality factor. The exciton-photon coupling constant appearing in Eqs. (16) is given by

$$\hbar g_{\mathbf{k}, \sigma} = -\langle \Phi_x, 0 | \frac{e}{mc} \mathbf{p} \cdot \mathbf{A}_{\mathbf{k}}^{\sigma} | \Phi_g, 1_{\mathbf{k}, \sigma} \rangle. \quad (17)$$

The coupling constant is related to the total oscillator strength per unit area $f_{\mathbf{k}}$ through

$$\sum_{\sigma=\text{TE, TM}} |g_{\mathbf{k}, \sigma}|^2 = \frac{2\pi e^2 \omega_x}{n_{\text{eff}} m c k L_c} f_{\mathbf{k}}. \quad (18)$$

Using the dipole approximation ($\mathbf{k}_e \approx -\mathbf{k}_h$), considering both polarizations and neglecting inter-subband mixing,

$f_{\mathbf{k}}$ is calculated to be

$$f_{\mathbf{k}} = |\tilde{\psi}(k_{\parallel})|^2 \left[\left(1 + \frac{k_z^2}{k^2} \right) \cos^2(k_z z) f_{\parallel} + \frac{k_{\parallel}^2}{k^2} \sin^2(k_z z) f_{\perp} \right] \quad (19)$$

where

$$f_{\parallel} = \frac{|\phi(0)|^2}{m\hbar\omega_x} |P_{cv} F_{e_{\parallel}}|^2 |\langle \chi_e | \chi_h \rangle|^2 \quad (20a)$$

$$f_{\perp} = \frac{|\phi(0)|^2}{m\hbar\omega_x} |P_{cv} F_{e_{\perp}}|^2 |\langle \chi_e | \chi_h \rangle|^2. \quad (20b)$$

In Eqs. (19-20) $\tilde{\psi}(k_{\parallel})$ is the in-plane Fourier transformed exciton CM wave function, $\phi(0)$ is the in-plane exciton relative motion wave function at zero, P_{cv} is the bulk transition matrix element, and $F_{e_{\parallel}}$ ($F_{e_{\perp}}$) is the parallel (perpendicular) polarization factor in quantum wells.²⁵

Integrating Eq. (16b) and substituting the resulting $c_{\mathbf{k},\sigma}(t)$ in Eq. (16a) we have the integro-differential equation

$$\dot{b}(t) = - \sum_{\mathbf{k},\sigma} |g_{\mathbf{k},\sigma}|^2 \int_0^t d\tau b(\tau) e^{[-i(\omega_{\mathbf{k}} - \omega_x) - \gamma_c/2](t-\tau)} - \frac{\gamma_x}{2} b(t). \quad (21)$$

In the weak coupling regime, which is clearly our case, $\gamma_c \gg g$ and one can solve Eq. (21) to a good approximation by taking $b(t)$ out of the integral. For $t \gg \gamma_c^{-1}$ the result is

$$\dot{b}(t) = - \frac{\gamma_x + \gamma_{SE}}{2} b(t) \quad (22)$$

where

$$\begin{aligned} \gamma_{SE} &= 2\pi \sum_{\mathbf{k},\sigma} |g_{\mathbf{k},\sigma}|^2 \mathcal{L}(\omega_{\mathbf{k}} - \omega_x, \gamma_c) \\ &= \frac{4\pi^2 e^2 \omega_x}{n_{\text{eff}}^2 m L_c} \sum_{\mathbf{k}} \frac{f_{\mathbf{k}}}{\omega_{\mathbf{k}}} \mathcal{L}(\omega_{\mathbf{k}} - \omega_x, \gamma_c), \end{aligned} \quad (23)$$

and

$$\mathcal{L}(\omega_{\mathbf{k}} - \omega_x, \gamma_c) = \frac{1}{2\pi} \frac{\gamma_c}{(\omega_{\mathbf{k}} - \omega_x)^2 + (\gamma_c/2)^2} \quad (24)$$

is the normalized Lorentzian cavity-mode broadening. The prime over the sum in Eq. (23) indicates taking the lowest cavity mode, $k_z = 2\pi/L_c$, and summing over the in-plane photon wave vectors, $\mathbf{k}_{\parallel} \leq q_x$, where $q_x = \omega_x/v$ is the maximum exciton in-plane wave vector that can still couple to the cavity mode resulting in radiative recombination of the exciton. The solution of Eq. (22) gives an exponential irreversible spontaneous emission of the exciton due to its coupling with the cavity field modes, representing Fermi's golden rule. As long as the calculated γ_{SE} is much smaller than the cavity broadening γ_c , the weak coupling approximation holds; otherwise, one must solve the general equation (21).

IV. RESULTS

We are interested in particular in the influence of the cavity on the exciton's spontaneous emission, radiative lifetime, and emission distribution.

A. Exciton Spontaneous Emission

Figure 2 shows the measured reflectivity of the cavity and the integrated photoluminescence intensity, using relatively high power, constant excitation. Each point in the figure results from emission from a distinct QD. The numerical aperture of our microscope objective in the PL measurements was 0.8, resulting in a collection angle of $\sim 13.2^\circ$ inside the sample. The figure shows a sharp dip in the reflectivity corresponding to the resonant cavity mode. The FWHM is 1.94meV giving a Q-factor of 670. The emission intensity shows a pronounced enhancement for QDs in resonance with the cavity mode. A rapid decrease in the emission intensity to a value roughly five times smaller is found for QDs detuned by 20 – 25meV

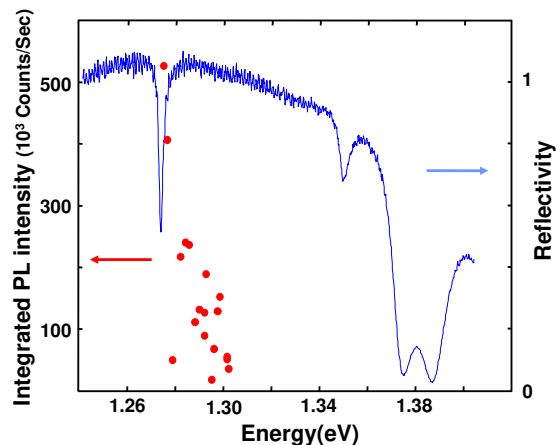


FIG. 2: (color online) Measured reflectivity (blue line) and integrated photoluminescence intensity (red points) of QDs at the antinode of a planar λ cavity.

In order to discuss these data, we relate the detuned exciton line to the λ cavity width by¹⁹

$$L_c = \frac{\lambda_x}{n_{\text{eff}}} \zeta = \frac{2\pi}{q_x} \zeta, \quad (25)$$

where ζ corresponds to the detuning of the exciton line from resonance. We assume the cavity resonant mode matches the emission from the heavy hole 1s exciton of a QD with a radius $R_D = 200\text{\AA}$, for which $\zeta = 1$. The corresponding resonance energy is calculated using Eq. (A-1) to be $E_x^{\text{res}} = E_c = 1.2756\text{eV}$. In order to model microscopically the emission from quantum dots that are detuned from this resonance, we represent the detuning by either changing the QD size or by changing the QD material bandgap (via the dot composition). The

dependence of the detuning on the QD radius is given in Fig. 1d. Considering only the basic cavity mode expressed as $k_z = q_x/\zeta$, Eqs. (23) and (19) are used to give

$$\gamma_{\text{SE}} = \frac{\pi e^2 \omega_x^2 R_D^2 f_{\parallel}}{m c^2 \zeta} \int_0^{q_x} dq q e^{-R_D^2 q^2/4} \frac{q^2 + 2q_x^2/\zeta^2}{(q^2 + q_x^2/\zeta^2)^{3/2}} \times \mathcal{L}\left(v\sqrt{q^2 + q_x^2/\zeta^2} - \omega_x, \gamma_c\right). \quad (26)$$

In deriving Eq. (26) we assumed that the QD resides in the center of the cavity, where the cavity mode takes its maximum value, and considered only the heavy-hole exciton whose perpendicular transition matrix element vanishes, $f_{\perp} = 0$. To account for the experimental collection angle, the upper limit of the integration in Eq. (26) is replaced with $q_0 = q_x \sin \theta$, where θ is measured from the z -axis.

In the calculation we used $n_{\text{eff}} = 3.5$, $\epsilon = 13.9$ resulting in QW exciton Bohr radius of $a_B = 116.7\text{\AA}$. The free (QW) exciton oscillator strength per unit area was calculated for a 30\AA $\text{In}_{0.53}\text{Ga}_{0.47}\text{As}$ QW and was found to be $f_{\parallel} = 7.1 \cdot 10^{-5} \text{\AA}^{-2}$.^{25,30} This value increases as the QD size reduces, due to the shrinkage of the relative motion wave function (see Eqs. 20). We took an additional factor of two for the oscillator strength to account for the two spin configurations.

In Figure 3 the calculated exciton spontaneous emission rates are shown together with the measured PL values as functions of exciton energy. The solid (blue) line corresponds to a calculation where detuning of the exciton energy was obtained by varying the QD radius whereas for the dashed (green) line the QD size was fixed to $R_D = 200\text{\AA}$ and its bandgap was varied. In order to put the measured and calculated values at the same figure, a scaling factor of 3000 was taken between the right (photon counts) and left (emission rate) axes. This factor corresponds to the photon extraction efficiency in the experiment, which was estimated from pulsed excitation measurements.³¹

The calculated results obtained by varying the dot size agree qualitatively with the experimental data, including the rapid fall off in the PL intensity away from resonance. The range of $90\text{\AA} \lesssim R_D \lesssim 300\text{\AA}$ that accounts for a detuning range of $\sim 20\text{meV}$ is consistent with variations in typical self-assembled InGaAs QDs. The two model calculations in Fig. 3 show marked differences. In particular, the emission enhancement shown for negative detuning in the case of variable QD size is missing in the fixed QD size calculation. The latter case shows a rapid inhibition of the emission as the QD becomes negatively detuned out of the cavity mode linewidth, which is clearly a cavity effect. In the case of variable R_D the cavity effect competes with the localization of the exciton CM wave function in \mathbf{k}_{\parallel} space, as the QD size increases [Eq. (26)]. This effect is consistent with the strong increase in QD exciton lifetime as compared with QW excitons. The competition between the cavity and localization effects is shown in the figure by the dip in the calculated emission

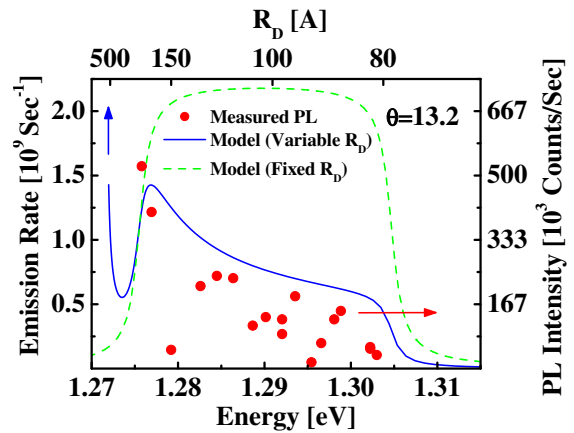


FIG. 3: (color online) Emission rates into a collection angle 13.2° vs. exciton energy. Full (red) circles are the measured values given in counts per second (right axis). Solid (blue) line shows the calculation where detuning is obtained by varying the QD radius (given in the top axis). Dashed (green) line shows the calculation with QD size fixed to $R_D = 200\text{\AA}$ and the detuning obtained by varying the QD material bandgap. A scaling factor of 3000 was taken between the left and right axes (see text).

rate (solid line) for $R_D \sim 300\text{\AA}$ (negative detuning). For yet larger QDs the localization effect takes over and the emission rate rapidly increases (the figure includes QDs with $R_D \leq 600\text{\AA}$). Such large QDs are less likely to form in our case and this increase is therefore not observed.

Figure 4 shows the dependence of the QD spontaneous emission on the excitation power. At low excitation the PL is dominated by a sharp emission line arising from the recombination of the 1s exciton. As the excitation power is increased, the dot populates with more carriers and recombinations of multiexcitons from higher collective states appear in the spectrum^{31,32}. For still higher excitation powers the emission is broadened and is extended beyond the cavity mode linewidth (see the reflectivity curve in Fig. 4). This is qualitatively confirmed by calculated emission rates that are superimposed over the high-excitation-power PL curve (topmost PL spectrum in Fig. 4). As before, the detuning of higher dot states is represented by either varying the dot size (solid blue line) or its material bandgap (dashed green line).

In Figure 5 we plot the experimental and calculated exciton lifetimes as functions of the emission spectral energy. Each point in the figure represents a measurement from a specific QD (open circles). The sample temperature during the measurements was 15K. The emission lifetime was estimated from a single exponential fit to the initial part of the measured PL decay curves (not shown). In general, the decay curves were quite sensitive to the excitation intensity and they were not single-exponentials. For the measurements we used excitation intensities which exactly saturate the PL emission. We note that there is a considerable scatter in the measured data. We believe that this scatter is mainly due to non-

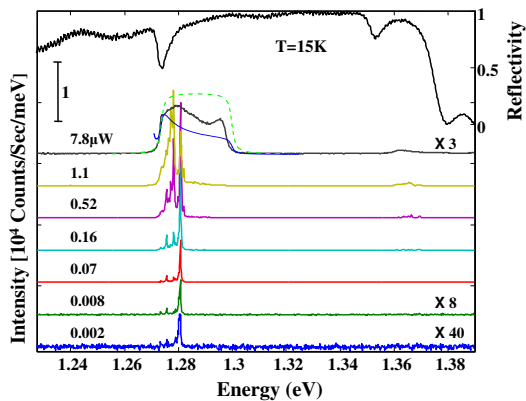


FIG. 4: (color online) Measured reflectivity (upper line) and integrated PL intensity for various excitation powers. Calculated emission rates with detuning by varying the QD radius (solid blue line) and its material bandgap (dashed green line) are superimposed on the measured PL with the highest excitation power.

radiative processes, which may depend on the particular environment and charge state of a given QD. Also, as mentioned above, the measured decay times were excitation intensity dependent. Our particular choice of excitation intensity, for which the exciton PL saturates, may be somewhat arbitrary. The saturation excitation may vary from one QD to the other in a way that has little to do with the microcavity.

For the model in which the detuning is represented by varying the QD material bandgap (dashed line), above resonance there are always cavity modes in the 2D continuum that can couple to the exciton due to the photon in-plane dispersion; thus the coupling remains effective even for a large positive detuning, resulting in a short recombination time. The emission from negatively detuned QDs is largely inhibited consistent with the experiment where emission from these QDs is not observed. This inhibition depends strongly on the cavity Q-factor and would be much less pronounced for weaker cavities. The calculations in which detunings are represented by varying the dot size (solid line) show a different behavior. When the QD radius is reduced (energies above resonance in Fig. 5) the lifetime increases due to the spread of the exciton CM wavefunction in k_{\parallel} space, as explained above. The very different lifetime behavior of the two detuning mechanisms may aid in identifying the various QDs. The results of both figures 3 and 5 seem to indicate that the majority of QDs have similar composition and their variations are mainly in size.

We note that the increase in radiative lifetime with reduction of the QD size is suppressed in the limit of strong confinement. This is because the oscillator strength (f_{\parallel}) increases due to the localization of the relative motion wavefunction. This effect is superseded by the breakdown of the selection rule caused by the spread of the CM k -space wavefunction outside q_x . Also note that the calculated linewidths due to spontaneous emission are at

most $\gamma_{SE} \lesssim 1.6 \mu\text{eV} \ll \gamma_c$ thus we are always in the weak coupling regime where our approximate solution is valid.

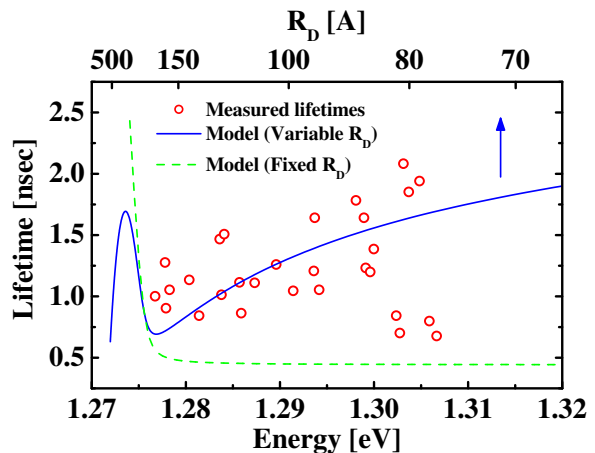


FIG. 5: Exciton radiative lifetime vs. its energy: open (red) circles are the measured values. Solid (blue) line shows the calculation where detuning is obtained with variable QD radius (given in the top axis). Dashed (green) line shows the calculation with QD size fixed to $R_D = 200 \text{ \AA}$ and its bandgap varied.

Next, angle resolved spectroscopy was performed on a single QD using high power excitation ($8 \mu\text{W}$). In these conditions the QD is populated with many carriers resulting in many available recombination channels. The PL spectrum therefore reflects the density of electromagnetic modes in the cavity. Fig. 6 shows a contour plot giving the measured PL intensity of a highly excited single QD, as registered by the CCD array camera at the exit of the monochromator. The horizontal axis gives the spectral dispersion while the vertical axis gives the angular distribution. Since the k_z part of the emission is fixed by the resonance condition to the cavity mode, this angle corresponds to the in-plane wave vector of the emission. From the geometry and lenses used for the imaging we estimate that each row in the CCD camera is equivalent to 0.38 mrad . The figure clearly demonstrates the in-plane dispersion of the cavity mode. The peaks in the emission intensity shown in the figure are most likely related to recombinations from various carrier configurations, e.g. the neutral and charged excitons, biexcitons and higher order multiexcitons^{31,32}, of the single QD. These multiexciton lines appear due to the high excitation power used in this experiment. Since our model accounts only for the neutral exciton line, we cannot compare our experimental data directly with the model calculations. Nevertheless, by taking the derivative of Eq. (26) with respect to the \mathbf{k}_{\parallel} space area (using $q = q_x \sin \theta$), we can achieve a similar in-plane dispersion of the cavity mode, as shown in Fig. 7. The models of QDs in which the size and the material bandgap were varied to represent the detuning show similar dispersion behavior. The difference between the two cases is mainly that in the case of fixed QD size the emission extends over a larger energy range (Fig. 7b),

which can be explained using the preceding arguments. We attribute the difference between the symmetric shape of the calculated angle resolved spectrum and the asymmetric shape of the measured one to the finite aperture of the confocal setup. The data was taken from a single QD that was positively detuned with respect to the MC resonance. Due to the relatively large spatial distribution of the emission from the QD (see section IV B), we could not collect the light from both negative and positive emission angles

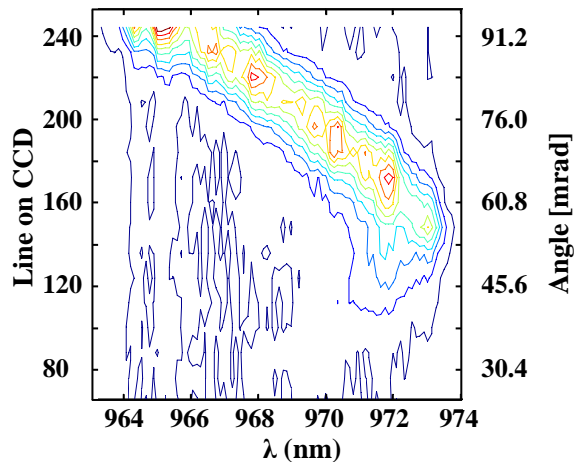


FIG. 6: (color online) Contour plot of the PL intensity from a highly excited single resonant QD in a planar microcavity as a function of photon wavelength and emission angle. Each contour represents 10% of the maximal intensity.

B. Spatial distribution of the Emission

We now turn to examine the in-plane spatial spread of a single QD emission. Fig. 8a shows a spatially integrated emission spectrum from a particular QD under moderate excitation power. Few discrete spectral lines are observed. Each spectral line corresponds to a particular emission line arising from the recombination of a ground state e-h pair from different many carriers' collective states.³² For our purpose it suffices to note that each line is spectrally detuned differently from the cavity mode. In order to estimate the spectral detuning of each line the reflectivity spectrum from this sample is overlaid on the emission spectrum in Fig. 8a. The least and most detuned lines are marked in the figure by A and by B respectively. Wavelength selective spatial images of the least (A) and most (B) detuned spectral lines are shown in Fig. 8b and Fig. 8c, respectively. The intensity distributions of the electromagnetic fields associated with the emission lines are essentially symmetric, though some obscuration, which can be partially attributed to mechanical drift, is present. The emission patterns contain a central strong spot surrounded by concentric rings with decreasing intensities. The intensities along the diagonals

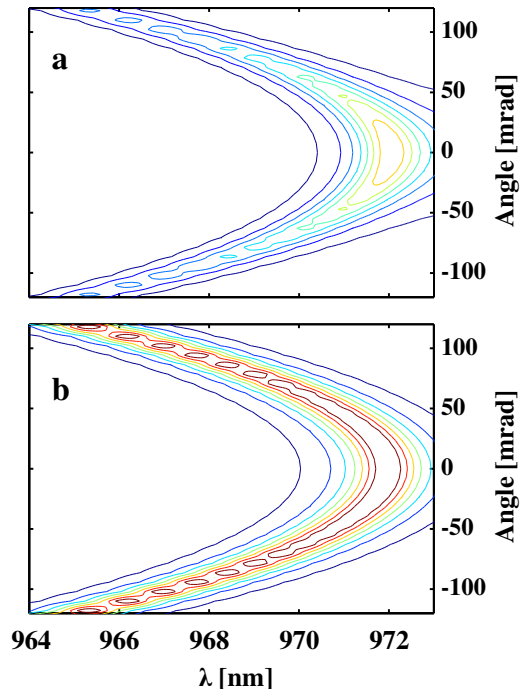


FIG. 7: Contour plot of the calculated emission rate distributions as a function of photon wavelength and emission angle (\mathbf{k}_{\parallel}). Each contour represents 10% of the maximal rate. Detuning is obtained by (a) varying the QD radius, and (b) varying the QD material bandgap and fixing the dot radius to $R_D = 200\text{\AA}$.

nals, which are marked by dashed (red) and solid (blue) lines in Figs. 8b and 8c, respectively, are displayed as functions of the in-plane distance from the image center in Fig. 8d.

Figs. 9a and 9b show the calculated images for the detunings of line A and line B respectively. Since both spectral lines originate from the same QD, we used different bandgaps to obtain the detuning. The images were generated by calculating the in-plane Fourier transform of the integrand in Eq. 23. The rates were calibrated so that their spatially integrated emission would match the calculated values given in Fig. 3. Fig. 9c shows the intensities along the diagonals of the calculated images as functions of the in-plane distance from the image center. In both measured and calculated images it is evident that when the QD is close to resonance with the cavity mode, its emission exhibits an in-plane spatial spread that is much larger than the QD size. The closer the emission energy to resonance is the larger is its spatial extent, and vice versa, the larger the detuning is, the more localized the emission pattern becomes. Calculated images, where detuning was modeled by varying the dot size, yielded similar behavior of the emission pattern, implying that the PL spatial spread is mainly a cavity effect depending only on detuning. In general, the calculated images agree with the experimental observations, both in their spatial

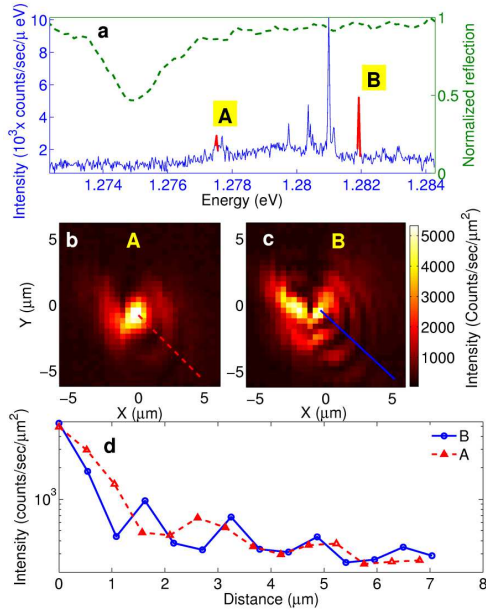


FIG. 8: (color online) (a) Spatially integrated emission spectrum measured from a single QD under moderate excitation power. The dashed (green) line shows the normalized reflection of the sample; Wavelength selective spatial image measured for (b) spectral line A; and (c) spectral line B; (d) Emission intensities along the diagonals which are marked by dashed (red) and solid (blue) lines as functions of the distance from the image center.

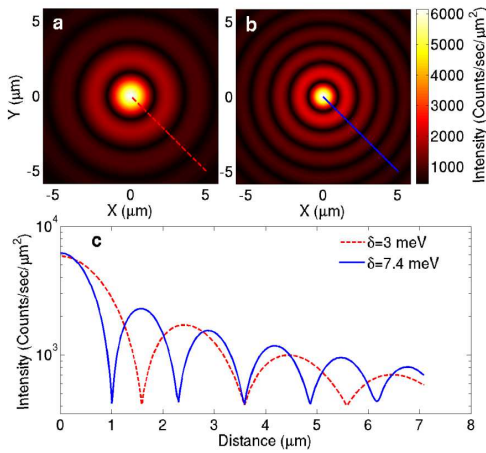


FIG. 9: (color online) Calculated spatial spread of the emission from a single QD detuned from resonance by (a) $\delta = 3$ meV; (b) $\delta = 7.4$ meV, corresponding to the measured spectral lines marked A and B in Fig. 8, respectively. Detuning is modeled by varying the QD material bandgap while the QD radius is fixed to $R_D = 200 \text{ \AA}$; (c) Calculated emission intensities as functions of the distance from the image center. (Constant background of 400 counts was added to the calculated emission to facilitate comparison with the measured data).

extent and in their dependence on the detuning, as can be concluded by comparing Fig. 9 with Fig. 8.

A discernible feature in Figs. 8d and 9c is the dependence of the spacing between the rings in the PL images on the detuning. The rings become more pronounced and denser for increasing positive detuning, where larger k_{\parallel} are needed for the emission. This gives rise to oscillations that are superimposed on the central emission line due to contributions arising from larger k_{\parallel} modes. The dependencies of the calculated locations of the 2nd and 3rd peaks on detuning are shown in Figure 10a, and their intensities normalized to the central peak are shown in Fig. 10b, confirming these observations. Identical results are obtained for both detuning models, suggesting again that this emission pattern is a cavity effect, depending only on detuning. Together with the central peak spread, the locations of the emission rings may aid in evaluating the QD's detuning. We note, though, that as Fig. 10b suggests, for spectral lines that are close to resonance with the cavity mode, the relative intensity of the rings emission to the central spot decreases rapidly, making them difficult to measure.

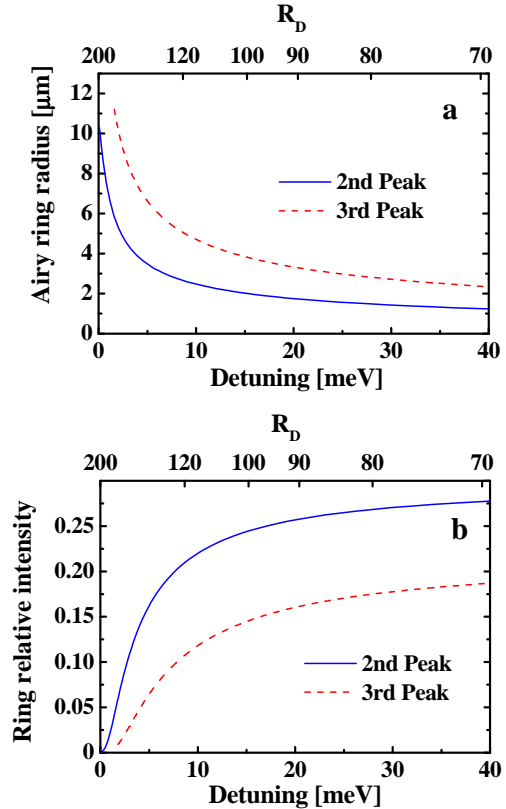


FIG. 10: (color online) (a) Calculated positions of second and third rings in the emission distribution; (b) Calculated emission intensity of second and third rings normalized to central emission peak.

V. SUMMARY

In this work we have studied the interaction between the electromagnetic modes in a planar cavity and excitons in single QDs embedded at the antinode of the cavity.

We find that the spontaneous emission outside the microcavity is enhanced considerably for dots in resonance with the cavity mode. The emission intensity rapidly decreases with detuning for lines that are positively detuned from the cavity mode. Emission from negatively detuned QDs is largely inhibited, and we were unable to observe any spectral emission below the cavity mode energy. Lifetime measurements have shown a decrease by a factor of roughly two for the lifetime of resonant QDs as compared with QDs that are 20 meV detuned from the cavity line. In-plane dispersion of cavity photons were directly observed by strong excitation of the QD, thereby transforming it into a broadband light source. Finally, we obtained near field images of the spatial emission distributions from single QDs, showing a large spread over several microns in the case of resonant QDs. These images have also shown emission rings with separation and

intensity that depend on the detuning of the QD from the cavity mode.

All of these features were qualitatively accounted for by calculations where detuning from the cavity mode was modeled by either varying the QD size or its bandgap. For most of the experimental data we have found better agreement with the first mechanism, suggesting that most of the QDs in strain driven self assembled samples vary in size rather than in composition. The range of $90\text{\AA} \lesssim R_D \lesssim 300\text{\AA}$ that accounts for the observed phenomena is consistent with typical self assembled InGaAs/GaAs quantum dots.

Acknowledgments

This work was supported by ONR, DARPA and the ONR Nanoscale Electronics Program. G. R. gratefully acknowledges the NRL/NRC Research Associateship. The work at the Technion was supported by the US-Israel Binational and by the Israeli Science Foundations.

Appendix

Here we provide some details of the calculation of the exciton's relative motion energy.

$$\begin{aligned}
E_r &= \langle \chi_e \chi_h \phi | H_r | \phi \chi_h \chi_e \rangle \\
&= 2\pi \mathcal{N}_r^2 (1 + \sigma) \frac{\alpha^2}{\eta^{2\alpha}} \int dr r^{2\alpha-1} e^{-2(r/\eta)^\alpha} + k_e^2 \mathcal{N}_{z_e}^2 \left[\sigma_{ez} \frac{L}{2} + \frac{V_e^z}{\kappa_e (k_e^2 + \kappa_e^2)} \right] + k_h^2 \mathcal{N}_{z_h}^2 \left[\sigma_{hz} \frac{L}{2} + \frac{V_h^z}{\kappa_h (k_h^2 + \kappa_h^2)} \right] - \\
&4\pi (\mathcal{N}_r \mathcal{N}_{z_e} \mathcal{N}_{z_h})^2 \int dr dq r J_0(qr) e^{-2(r/\eta)^\alpha} \sum_{i=1}^4 \mathcal{I}_i(q) + \frac{8\pi \mathcal{N}_r^2 \sigma^2}{(1 + \sigma)^3 \xi^4} \int dr r^3 e^{-2(r/\eta)^\alpha}. \tag{A-1}
\end{aligned}$$

$\mathcal{I}_i(q)$ are given by

$$\begin{aligned}
\mathcal{I}_1(q) &= \frac{L}{2q} + \frac{1}{4q^2} \left[\sum_{i=e,h} \frac{g_i}{k_i^2} + \sum_{i \neq j} \frac{g_i}{k_i^2 - k_j^2} \left(\frac{f_j}{q^2 + 4k_e^2} - 1 \right) \right] - \\
&e^{-qL/2} (f_e - g_e) \frac{\cosh(qL/2)g_h + \sinh(qL/2)f_h}{q^2(q^2 + 4k_e^2)(q^2 + 4k_h^2)} \tag{A-2a}
\end{aligned}$$

$$\mathcal{I}_2(q) = \frac{2k_e^2 e^{-qL/2} \sinh(qL/2)f_h + \cosh(qL/2)g_h}{k_e^2 + \kappa_e^2} \frac{1}{q(q + 2\kappa_e)(q^2 + 4k_h^2)} \tag{A-2b}$$

$$\mathcal{I}_3(q) = \frac{2k_h^2 e^{-qL/2} \sinh(qL/2)f_e + \cosh(qL/2)g_e}{k_h^2 + \kappa_h^2} \frac{1}{q(q + 2\kappa_h)(q^2 + 4k_e^2)} \tag{A-2c}$$

$$\mathcal{I}_4(q) = \frac{4k_e^2 k_h^2}{(k_e^2 + \kappa_e^2)(k_h^2 + \kappa_h^2)} \frac{\kappa_e + \kappa_h + q}{(\kappa_e + \kappa_h)(2\kappa_e + q)(2\kappa_h + q)} \tag{A-2d}$$

where

$$f_i = 4k_i^2 + q^2 + q^2 \cos(k_i L) \quad , \quad g_i = 2qk_i \sin(k_i L). \tag{A-3}$$

-
- * Electronic address: guy.ramon@gmail.com; Current address: Department of Physics, University of Buffalo, SUNY, Buffalo, NY 15260-1500
- ¹ P. Michler, A. Imamoglu, M. D. Mason, P. J. Carson, G. F. Strouse, and S. K. Buratto, *Nature (London)* **406**, 968 (2000); C. Santori, M. Pelton, G. Solomon, Y. Dale, and Y. Yamamoto, *Phys. Rev. Lett.* **86**, 1502 (2001); D. V. Regelman, U. Mizrahi, D. Gershoni, E. Ehrenfreund, W. V. Schoenfeld, and P. M. Petroff, *ibid* **87**, 257401 (2001).
 - ² A. Kiraz, M. Atatüre, and A. Imamoglu, *Phys. Rev. A* **69**, 032305 (2004).
 - ³ E. Knill, R. Laflamme, and G. J. Milburn, *Nature (London)* **409**, 46 (2001).
 - ⁴ C. Santori, D. Fattal, J. Vučković, G. S. Solomon, and Y. Yamamoto, *Nature (London)* **419**, 594 (2002).
 - ⁵ K. J. Vahala, *Nature (London)* **424**, 839 (2003).
 - ⁶ J. M. Gérard, B. Sermage, B. Gayral, B. Legrand, E. Costard, and V. Thierry-Mieg, *Phys. Rev. Lett.* **81**, 1110 (1998).
 - ⁷ M. Pelton, C. Santori, J. Vučković, B. Zhang, G. S. Solomon, J. Plant, and Y. Yamamoto, *Phys. Rev. Lett.* **89**, 233602 (2002).
 - ⁸ B. Gayral, J. M. Gérard, A. Lemaître, C. Dupuis, L. Manin, and J. L. Pelouard, *Appl. Phys. Lett.* **75**, 1908 (1999).
 - ⁹ T. Yoshie, A. Scherer, J. Hendrickson, G. Khitrova, H. M. Gibbs, G. Rupper, C. Ell, O. B. Shchekin, and G. Deppe, *Nature (London)* **432**, 200 (2004).
 - ¹⁰ J. P. Reithmaier, G. Sek, A. Löffler, C. Hofmann, S. Kuhn, S. Reitzenstein, L. V. Keldysh, V. D. Kulakovskii, T. L. Reinecke, and A. Forchel, *Nature (London)* **432**, 197 (2004).
 - ¹¹ A. Badolato, K. Hennessy, M. Atatu(re), J. Dreiser, E. Hu, P. M. Petroff, A. Imamoglu, *Science* **308**, 1138 (2005).
 - ¹² L. C. Andreani, G. Panzarini, and J-M. Gérard, *Phys. Rev. B* **60**, 13276 (1999).
 - ¹³ G. Björk, S. Machida, Y. Yamamoto, and K. Igeta, *Phys. Rev. A* **44**, 669 (1991).
 - ¹⁴ A. J. Bennett, D. C. Unitt, P. See, A. J. Shields, P. Atkinson, K. Cooper, and D. A. Ritchie, *Appl. Phys. Lett.* **86**, 181102 (2005).
 - ¹⁵ C. Weisbuch, M. Nishioka, A. Ishikawa, Y. Arakawa, *Phys. Rev. Lett.* **69**, 3314 (1992)
 - ¹⁶ V. Savona, Z. Hradil, A. Quattropani, and P. Schwendimann, *Phys. Rev. B* **49**, 8774 (1994).
 - ¹⁷ V. Savona, F. Tassone, C. Piermarocchi, A. Quattropani, and P. Schwendimann, *Phys. Rev. B* **53**, 13051 (1996).
 - ¹⁸ D. S. Citrin *IEEE J. Quant. Elec.* **30**, 997 (1994).
 - ¹⁹ M. Sugawara, *Jpn. J. Appl. Phys.* **36**, 2151 (1997).
 - ²⁰ J. T. Andrews, P. Sen, and R. R. Puri *J. Phys. Cond. Matt.* **11**, 6287 (1999).
 - ²¹ C. Y. Hu, H. Z. Zheng, J. D. Zhang, H. Zhang, F. H. Yang, and Y. P. Zeng, *Appl. Phys. Lett.* **82**, 665 (2003).
 - ²² J. M. Garcia, T. Mankad, P. O. Holtz, P. J. Wellman, and P. M. Petroff, *Appl. Phys. Lett.* **72**, 3172 (1998).
 - ²³ W. Que, *Phys. Rev. B* **45**, 11036 (1992).
 - ²⁴ For a general lateral poetential, seperation of the CM- and relative-motions is valid only when the QD radius is much larger than the exciton Bohr radius.
 - ²⁵ M. Sugawara, *Phys. Rev. B* **51**, 10743 (1995).
 - ²⁶ R. L. Greene, K. K. Bajaj and D. E. Phelps, *Phys. Rev. B* **29**, 1807 (1984).
 - ²⁷ M. Grundmann and D. Bimberg, *Phys. Rev. B* **38**, R13486 (1988).
 - ²⁸ D. Gershoni, C. H. Henry, and G. A. Baraff, *IEEE journal of quantum electronics* **29**, 2433 (1993).
 - ²⁹ J. D. Jackson, *Classical Electrodynamics*, 2nd edition (John Wiley, New York, 1975).
 - ³⁰ L. C. Andreani and A. Pasquarello, *Phys. Rev. B* **42**, 8928 (1990).
 - ³¹ E. Dekel, D. Gershoni, E. Ehrenfreund, J. M. Garcia, and P. M. Petroff, *Phys. Rev. B* **61**, 11009 (2000).
 - ³² E. Dekel, D. Gershoni, E. Ehrenfreund, D. Spektor, J. M. Garcia, and P. M. Petroff, *Phys. Rev. Lett.* **80**, 4991 (1998).